Fuel 381 (2025) 133172

Contents lists available at ScienceDirect

Fuel

journal homepage: www.elsevier.com/locate/fuel

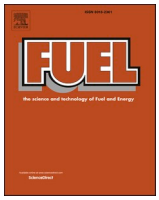

Full Length Article

Evaluation of the effect of a biomass fuel source on the thermal properties of iron ore sinter

Sam Reis [a,*], Peter J. Holliman [a], Ciaran Martin [b]

[a] Swansea University, Singleton Park, Swansea SA2 8PP, UK
[b] Tata Steel UK Ltd, Port Talbot, Swansea SA13 2NG, UK

ARTICLE INFO

Keywords:
Ironmaking
Thermography
Heat transfer
Decarbonisation
Energy efficiency

ABSTRACT

The knowledge around the effect of bioenergy on the thermal properties of iron ore sinter is not widely understood. Therefore, the effects of a 30 % biomass hybrid was investigated. Experiments placed samples in thermal environments encapsulating radiant, convective and conductive heating at increasing thermal gradients. Temperature data was collected using a longwave IR thermal camera, prompting a gap in literature knowledge – "Does emissivity vary as sinter undergoes thermal change?" to be studied. Furnace data in the range of 200 °C–600 °C showed an increasing trend in emissivity from 0.82 to 0.93 with a deviation of <2 % between 0 and 100 % hybrid samples. The results of the subsequent thermal tests indicated an initial barrier to energy absorption caused by the morphology of the sinter that decreased with the thermal gradient. Statistical analysis concluded that the 75 % blend, absorbed energy at a consistently high rate in all the heating environments. Linear regression analysis with x-ray fluorescence and diffraction data showed that the quantity of FeO, prismatic SFCA and platy SFCA had a measurable effect on the heating rate at 400 °C. However, as temperatures increased to 600 °C Fe_2O_3 had more effect than FeO, with the SFCA phases maintaining their impact on heating rate.

1. Introduction

Blast furnaces are still the primary method of steel production despite a global shift towards electric (EAF) and hydrogen steelmaking (H-DRI), with 63 % of global crude steel production and 57 % of planned production [1]. The utilisation of sinter in the BF is highly efficient [2]. But sintering's dependence on fossil fuels and their subsequent harmful emissions is the primary driver of increased planned EAF and H-DRI capacity [3]. However, due to BF being the majority of planned steelmaking capacity, increased research to reduce their environmental impact is still very much needed. The current literature regarding the optimisation of sinter production and its use in the blast furnace is extensive, containing almost 1000 papers [4]. Two ways of reducing the environmental impact of the BF steelmaking process are switching fossil fuels for more sustainable biofuels [5] and reducing the total energy consumption [6–9]. Reducing consumption relies on using supplied energy more efficiently. A significant portion of energy is lost by cooling the sinter and reheating it in the blast furnace [10]. While the sinter must cool to form critical phases responsible for strength and reducibility [11], the released energy can be absorbed and recycled to offset the need for primary energy input. Therefore, determining if using biofuels negatively affects the thermal properties of the sinter is crucial to more efficient use of energy in the cooler and BF. Substitution of fossil fuels with biofuels in the sintering process has been promising, producing significant reductions in fossil fuel use. Lovel et al. [12] compared coke with mass-produced charcoal and a small batch of black pine charcoal. They found that the charcoals had a higher calorific value than the cokes, but increased fuel rates were required to create high-quality sinter. Runs using 100 % charcoal increased productivity due to its higher reactivity but produced sinter with a lower strength. Consequently, a blend of coke and charcoal created a balance. Xiaohui et al. [13] found that using straw-derived biochar in a laboratory sinter pot could replace fossil fuel at a maximum rate of 20 %, defined by product quality declining below target levels. The process of preforming the biochar at 200 °C under 120 MPa of pressure for 60 s more than doubled the energy density of the biochar and increased maximum biomass replacement to 40 %. Zhao et al. [14] used a 2D sintering model to simulate the process and arrived at a similar conclusion to Lovel et al. that charcoal could replace 10–15 % of the fossil fuel. However, when it was coated in fine iron ore, the acceptable

* Corresponding author.
E-mail address: 902162@swansea.ac.uk (S. Reis).

https://doi.org/10.1016/j.fuel.2024.133172
Received 25 January 2024; Received in revised form 30 August 2024; Accepted 14 September 2024

replacement increased to 30 %. Overall, it is apparent that producing high-quality sinter is possible using a proportion of biomass as an energy carrier. It has been identified that sinter strength is derived from the formation of bonding phases [15]. These phases are known as silico ferrites of calcium and aluminium (SFCA) and form at high temperatures through solid–liquid reactions in the melt and crystallisation as the melt cools [16,11]. The maximum temperature produced by the fuels also affects the distribution of iron oxides within the sinter [17]. These oxides constitute the majority of the mass of the sinter and potentially the bulk of its thermal properties. An increase in FeO increased the energy required to reduce the sinter in addition to an increase in magnetite and a decrease in hematite. Additionally, a higher level of fine SFCA increased sinter strength which is linked with sinter retaining its structure as it heats, therefore reducing energy consumption [18]. Studies by Li et al. [19] and Zöll et al. [20] described the heat capacity of platy and prismatic SFCA accordingly. These studies found that the heat capacities were much lower than iron oxides, indicating they could conduct excess energy to the oxides thus resulting in a faster heating rate. Donskov, Lyalyuk and Donskov [21] investigated the energy efficiency of the BF and how to increase it. Their analysis found that fuel consumption was reduced by increasing heat utilisation and suppressing direct reduction 58 by lowering FeO content in the burden.

Loo et al. [10] compared the impact of softening and melting properties of the burden on energy consumption. It was found that reducing the temperature difference between softening and melting lowered the pressure drop and subsequent energy consumption. The authors concluded that fibrous silico ferrite of calcium and aluminium (SFCA) present in the sinter was critical in increasing softening temperature and reducing energy consumption.

In this paper, we evaluate the thermal properties of iron ore sinter made using increasing levels of a hybrid biofuel, ecoke® (CPL, Immingham) containing 30 % biomass. A long-wave IR thermal camera was used to evaluate the emissivity and temperature of the samples. Both macroscopic and microscopic observations were made to investigate their effect on the thermal properties. To the best of our knowledge, a study of this kind has not been reported in the literature utilising infrared thermography to evaluate sinter made using biofuels. We believe that these data can be used to improve heat transfer rates in the blast furnace and the sinter cooling process.

2. Materials and methods

The sinter samples used in this study were made under laboratory conditions using the pilot sinter pot at the Port Talbot steelworks [18]. The energy sources used were Port Talbot coke breeze (denoted PT breeze in this paper) and a hybrid fuel composed of 30 % sustainably sourced biomass and 70 % anthracite, branded as, ecoke® (CPL ltd, Immingham). The sinter samples were made using increasing quantities of ecoke® from 0 to 100 % in 25 % increments. A summary of previous investigations of calorific and kinetic combustion properties by the authors [22] can be seen in Table 1. Briefly, this previous paper investigated the fuels used to make the samples in this study to validate their ability to replace PT breeze within the sinter pot. It was found that ecoke® had a much higher volatile content and lower burnout temperature, but a slightly larger calorific value than the PT breeze. Therefore, in the confined conditions of the sinter pot ecoke® would provide the required energy to create high-quality sinter. Compositional analysis of the fuels using energy dispersive spectroscopy (EDS) is displayed in Table 2. The carbon content of both fuels was remarkably similar but the ecoke® had a much lower sulphur, silicon and aluminium content but a higher potassium and calcium content than the PT breeze. Differences in silicon and calcium content impacted the quantity of flux required in the blend. The high sulphur content of the PT breeze could potentially create impurities in the sinter and increase SO_2 emissions. For each fuel ratio, 4 equally sized pieces of sinter were selected from the 16–25 mm fraction for thermal testing. From these samples, two were chosen randomly to be reduced to a particle size of < 20 μm using a Retsch RS200 vibratory disk mill. Lump samples were imaged from all sides using a 50mp camera, mounted on a tripod for consistency Fig. 1. The images were imported into Fiji (Image J2) where the pixel to mm ratio was determined using the scale. Subsequently, 3 repeat measurements were taken for each image to account for the variability in the sinter. From these dimensional measurements, surface area, volume, and length could be calculated to analyse their impact on the thermal properties. The dimensions for the different pieces of sinter measured through the image J method had a maximum standard deviation of 14 % half the percentage difference from 16-25 mm indicating a good selection of samples.

Table 1
A summary of the proximate analysis, bomb calorimetry and thermogravimetric analysis conducted in [22].

Sample	FC %	VM %	A %	CV MJ/kg	Burnout °C
ecoke®	78.7	13.3	8.9	27.9	523
PT Breeze	83.4	7.4	9.2	26.5	724

Iron ore sinter must pass strict quality barriers to maximise its efficiency in the blast furnace. The core metrics are the strength and reducibility of the sinter. Firstly, the iron ore sinter must retain its structure on transfer to and in the blast furnace to maintain a small pressure drop. Secondly, the iron ore sinter must have a high rate of reduction to lower fuel consumption in the blast furnace. The pre-reduction strength of the sinter is measured by calculating the yield of iron ore sinter > 5 mm, after undergoing high levels of impact and abrasion in a mechanical sieve. The rate of reduction was calculated at 900 °C in a CO/CO2 atmosphere, ISO-7215. Post-reduction strength testing, a continuation of ISO-7215, tumbled the sinter (impact and abrasion) for 300 s before size classification. The results of these tests, Table 3, showed that a comparable yield of sinter (up to 71.6 % versus 63.2 % for PT breeze) was produced using ecoke® although the sinter reduced slower than the 100 % PT breeze. However, the sinter made with ecoke® had a higher post-reduction strength. Finally, sinter made with ecoke® had a higher ratio of SFCA to hematite because of the longer melt time.

2.1. Thermal camera data processing

The extraction of temperature data from the thermal images and videos was done using FLIR research studio (Teledyne FLIR LLC). Firstly, the experimental parameters were set, including the distance from the lens, air temperature, humidity and emissivity. Infrared radiation reduces in intensity by the square of the distance in addition to being scattered by the air, thus reducing the intensity further as air temperature and humidity increase [23]. Therefore, the measurement of these parameters allows the camera to compensate thus, increasing the measurement accuracy. Next, point or area selections were used, dependent on the tests, and the results were exported into Excel (Microsoft). The overall heating rate was calculated using equation (1), with T_2 = final temperature, T_1 = initial temperature, t_2 = end time and $t_1 = 0$ along with point-to-point heating rates with T_2 = temperature at $t_1 + x$, T_1 = temperature at t_1, $t_2 = t_1 + x$ and $t_1 = t_1$ where x = chosen time interval. Experiments where recordings instead of still images were taken, namely the firebox and hot plate, had a lot of noise in their point-to-point heating rates calculations. Therefore, recordings were smoothed using adjacent averaging as this was the simplest method to reduce noise and retain the shape of the data. All the heating rates were normalised using equations (2) and (3) where A_s and V_s are the area and volume of the sinter respectively, subsequently A_M and V_M were the maximum values in the respective set.

$$\frac{dT}{dt} = \frac{T_2 - T_1}{t_2 - t_1} \tag{1}$$

Table 2
EDS data for ecoke® and PT breeze.

Material	CaO	SiO_2	MgO	Al_2O_3	P	S	Na_2O	K2O	C
PT breeze	0.92	5.66	0.25	2.94	0.09	0.71	0.07	0.16	85.85
ecoke®	1.47	1.92	0.22	0.77	0.07	0.05	0.67	0.00	81.70

Table 3
Selected data on sinter quality for material sintered using ecoke:PT breeze ratios of 0:100 (EC0), 25:75 (EC25), 50:50 (EC50), 75:25 (EC75) and 100:0 (EC100). CP = Cold permeability, MT = Melt time, He = Hematite.

Run	CP (m^3/hr)	MT (s)	Yield (%)	Reduction (min)	Disintegration (%)	He/SFCA (% / %)
EC0	8.26	7.4	63.2	129.0	35.5	2.32
EC25	8.32	14.8	71.6	132.2	26.4	2.53
EC50	7.87	11.9	60.0	145.2	22.0	2.89
EC75	8.67	9.2	69.2	136.7	24.8	1.99
EC100	8.50	3.9	59.8	125.0	40.0	2.38

$$\frac{dT}{dt} = \frac{T_2 - T_1}{t_2 - t_1} \times \frac{A_s}{A_m} \tag{2}$$

$$\frac{dT}{dt} = \frac{T_2 - T_1}{t_2 - t_1} \times \frac{V_s}{V_m} \tag{3}$$

2.2. Emissivity calculation

The emissivity of an object has been defined as the ratio between the energy radiated from an object and that of a blackbody [24]. Very few sources quote the emissivity of iron ore sinter, Usamentiaga et al. [25] used a value of 0.9 to track the temperature of sinter in a rotary cooler. Castro, Sazaki and Yagi [26] simulated the sintering process using a value of 0.8. To evaluate the emissivity of the sinter samples at different temperatures, they were placed in the furnace at 200 °C,400 °C and 600 °C, respectively. Thermal images were captured after 1 h and then in 30-minute intervals up to 2.5 h. In FLIR Research Studio, equal-sized areas the size of the smallest sample,44x28 pixels, were drawn on each sample to calculate the maximum, minimum and average temperatures. Subsequently, the emissivity was adjusted within the software so that the maximum temperature for each piece of sinter was within a 2 % margin of error concerning the furnace temperature, Fig. 2.

2.3. Furnace method

To evaluate the sinter samples' radiative and convective properties they were placed in a Carbolite ELF laboratory furnace set at 400 °C and 600 °C, respectively. An initial thermal image was captured, at t = 0 with subsequent images taken every 30 s. The 400 °C and 600 °C tests were run for 8 and 16 min accordingly to allow the samples to obtain a steady temperature, thus enabling a fair comparison. Fig. 3 shows the layout of the furnace, firebox and hotplate and the source of the IR radiation in each. The use of the furnace enabled even heating of the samples due to the placement of the heating coils and the reflective properties of the lining.

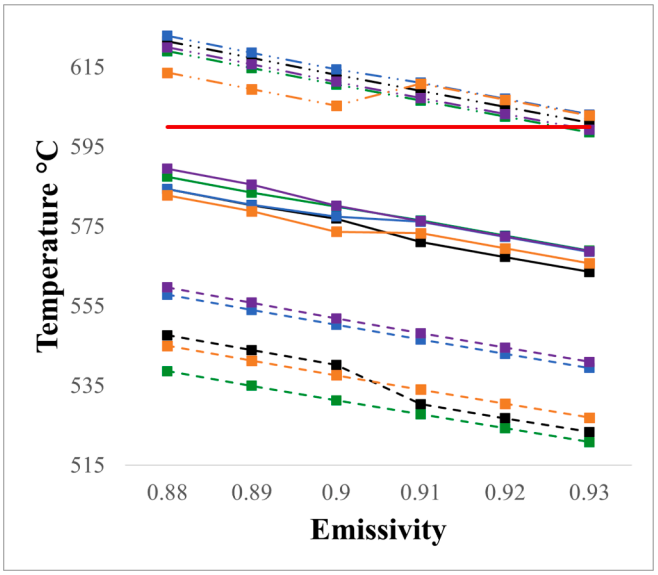

Fig. 2. A plot of emissivity vs temperature (where dotted line = minimum, solid line = average and dot dashed line = maximum) for each sample, Orange = EC100, Purple = EC75, Blue = EC50, Green = EC25, Black = EC0.

2.4. Firebox method

To test the high-temperature conductive thermal characteristics of the samples, a specialised piece of equipment, referred to as a firebox, was used. The equipment comprised a fireproof chamber containing an adjustable propane burner and an extraction hood. Samples were suspended over the flame using a metal clamp to consistently position the

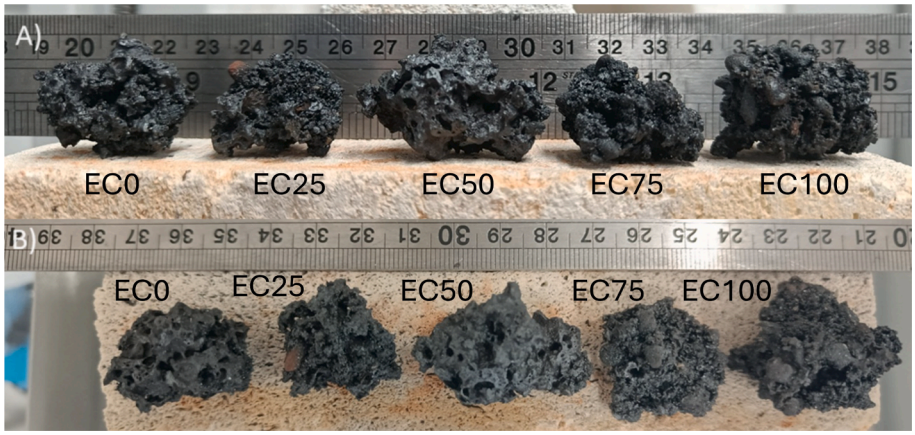

Fig. 1. Sinter samples. A = front on view of sinter samples, B = top down view of sinter samples. Left to right EC0-100.

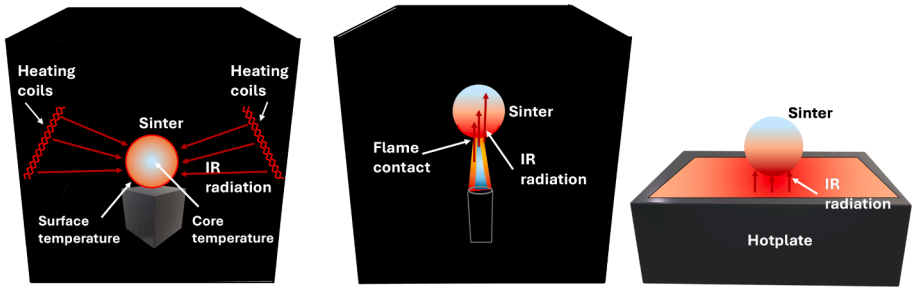

Fig. 3. Schematic of furnace (left), Firebox (middle) and hotplate (right) heating methods used in this work and the predicted temperature gradient (red to blue) within the samples.

sample at the tip of the flame. Heat flow through the samples was measured using the A700 thermal camera, positioned perpendicular to the sinter. The propane flame ca.2000 °C was positioned under the samples for 1.5 min. Fig. 3 shows that the heat was transferred to the sample via conduction from the flame and infrared radiation from the combustion gases.

2.5. Hotplate method

To simulate thermal conduction at a reduced thermal gradient, 550 °C compared to 2000 °C, a high-temperature hotplate with a 1 °C accuracy was used. To investigate the effect of chemical and mineralogical composition 0.5 g of powdered samples were formed into 2.5 cm squares with a depth of 5 mm on a square of aluminium foil. The samples were then placed onto the hotplate, set at 400 °C and 550 °C for 4 min. In this experiment, the camera was set vertically above the samples to identify the rate of conduction through the height of the sample. Fig. 3 shows that heat was transferre by conduction through the hotplate and into the bottom of the samples.

3. Results and discussion

3.1. Emissivity

Fig. 2 displays the results of this experiment for 600 °C and shows a negative correlation between emissivity and perceived temperature on the camera. Table 5 shows that at an emissivity of 0.93, the average of the maximum temperatures of the samples was 601 °C and the standard deviation was 2.0 °C. To identify the cause of the spread of temperatures, the maximum, minimum and average temperatures were compared to XRD and XRF data, Table S1-2. The results showed that SFCA correlated the most with the minimum temperatures, but hematite and magnetite had the best correlation with the maximum temperatures. Therefore, the formation of SFCA reduces the emissivity. Thermal cameras do not directly measure the temperature of an object but instead, calculate it based on the number and energy of incident photons. Therefore, the difference in the bandgap, and therefore emissivity, between SFCA and magnetite present at the surface of the sinter produced photons with different amounts of energy thus displaying a different temperature [27]. Secondly, because of the concave and convex features on the surface of the sinter, the photons are reflected off the surface before entering the detector thus affecting their energy and the calculated temperature. A method to correct this is to quantify the texture of the surface using 3D imaging [28] and use the spacial coordinates to modify the emissivity. Fig. 4 shows a positive trend between emissivity and actual temperature, with samples behaving more like a blackbody radiator whereby increased amounts of energy were being radiated from the samples. This could be explained by the change band gaps of the oxides as haematite (ca. 2.2 eV, [29]) changes to magnetite (1.8 eV, [30]) and then to wüstite (1.9 eV, [31]). These phase changes would also shift the onset of radiation absorption from $\lambda_{onset} = 563$ nm to 688 nm to 652 nm, respectively, i.e., from visible light to infrared light. This result shows sinter made using ecoke® at 600 °C could transfer heat very efficiently to other objects, therefore improving the theoretical efficiency for the recycling of energy in the process. In their work, Usamentiaga et al. [26] used a linear scale with a maximum temperature of 500 °C using the results in Table 5 an emissivity of 0.90 correlates well with our data.

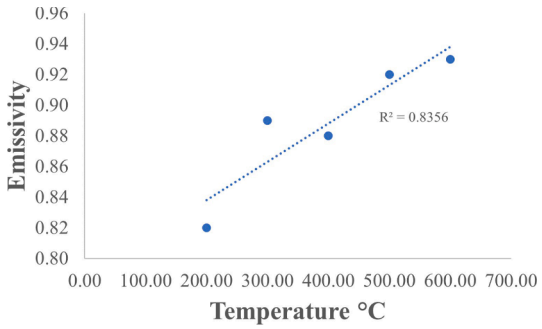

Fig. 4. The average trend of the emissivity of lump sinter samples with temperature.

3.2. Furnace

The temperature and heating rates for the 400 °C and 600 °C furnace tests are presented in Fig. 5a-c and 6a-c. These figures show the temperature progression of the samples and their respective heating rates and volume-adjusted heating rates equations (2) and (3). Firstly, analysing Fig. 5a, the temperature profile of each sinter sample was an asymptotic curve reaching the limit at 400 °C by approximately 240 s. Heating rates at 120 s in Fig. 5b, showed that EC75 and 50 had the highest heating rate at 55 and 54°C/min respectively. 120 s was chosen as it was the midpoint of the heating section and gave a good representation of the differences in the samples.

Moving to the volume-adjusted heating rates, Fig. 5c, EC50 had the highest heating rate with a value of 54 °C/min followed closely by EC75. After a large gap, 25 °C/min, the subsequent order remained the same where EC0 and EC100 had the highest values of 29 and 26 °C/min and EC25 the lowest at 21 °C/min. The distribution of heating rates in using equation (3) was 80 °C/min compared with 55 °C/min for equation (2) at 30 s. Although, this drops to 30 and 34 °C/min by 120 s. This data shows that the sample's dimensions affected the initial heat absorption but diminished as heating continued. Linear regression analysis determined the impact of different mineral structures and chemical elements on the unmodified heating rate. Subsequently, the FeO percentage had a significant influence on the heating rate with an R-score of 0.94. Prismatic and platy SFCA also influenced the heating rate with R-scores of 0.86 and 0.73. Despite having a lower emissivity, SFCA improves the heat transfer properties of the sinter, but a dense crystal structure is not as desirable when absorbing IR radiation.

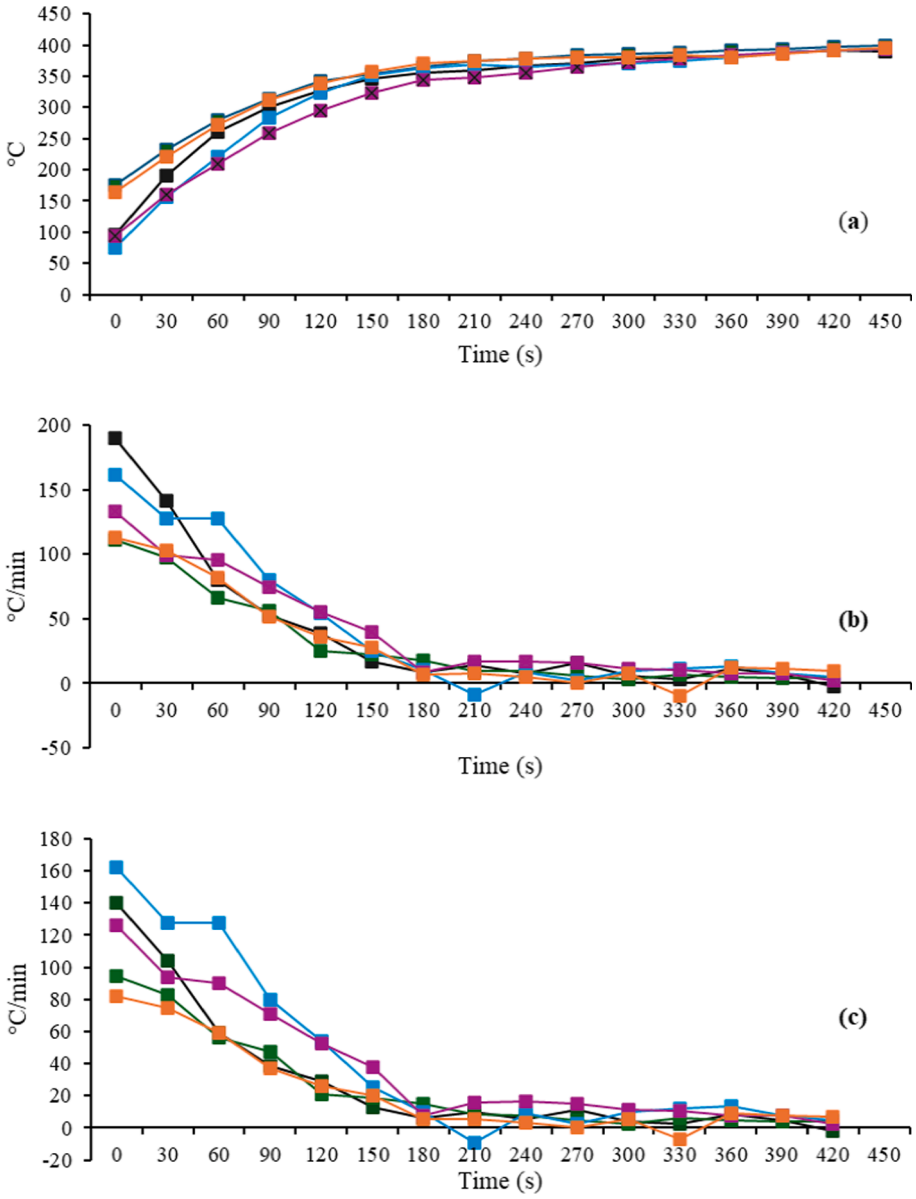

Fig. 5. Steady state furnace set at 400 °C Orange = EC100, Purple = EC75, Blue = EC50, Green = EC25, Black = EC0 where a = Sample temperatures recorded every 30 s b = heating rate calculated in 30 s intervals c = heating rate adjusted for volume calculated in 30 s intervals.

At 600 °C, Fig. 6a, shows that maximum temperatures were reached by 450 s. Analysing the results of the standard heating rate calculation at 210 s, Fig. 6b, showed a very narrow distribution of heating rates, 12 °C/min, excluding the anomalous points attributed to a slight error in the timing of capturing the thermal image. After 210 s, EC0 had the highest heating rate with a value of 23 °C/min followed by EC100, EC25, EC50 and EC75; an order almost the opposite to the 400 °C tests. A shift from FeO having the most effect on heating rate, at 400 °C, to Fe_2O_3 at 600 °C could explain this. FeO showed a negative correlation with heating rate and Fe_2O_3 a positive.

Analysing the distribution of Fe_2O_3 and FeO EC100 and EC0 had comparatively large values for both. Prismatic SFCA still correlated but with a reduced R-score of 0.61. Unlike the 400 °C test, the calculated volume and area Table 4 had relatively significant R-scores, 0.52–0.68, showing an increase in thermal gradient resulted in physical dimensions having a greater effect on the heating rate. An increased surface area absorbed the incident radiation from the furnace more efficiently. The correlation of heating rate with surface area and volume is only seen with the average heating rates, thus backing up this theory. The results of these tests show that sinter made using ecoke can effectively absorb radiated heat proving its suitability for use in the blast furnace. Additionally, the results show the energy contained can be recycled by utilising convection.

Adjusting for the dimensions of the sinter, Fig. 6c at 210 s EC100 topped the heating rate at 19 °C/min followed by EC0, EC75, EC25 and EC50. Interestingly EC50 had the lowest heating rate in contrast to the 400 °C tests. EC25 remained near the lowest rate, and EC0 and EC75 near the top. The spread of heating rates was a third of the 400 °C run at 10 °C/min validating the theory of an initial barrier to heat transfer. At 90 s the order slightly changed, with EC75 having a rate of 96 °C/min followed by EC100, EC0, EC50 and EC25. The range of the heating rates was much higher at 47 °C/min making these results more comparable to the 400 °C run. These results suggest that in the early heating stages, the heating rates were dependent on the size and composition of the sinter but became less dependent as the temperature increased. As the thermal gradient through the sinter reduces the resistance of individual phases becomes the limiting factor consistent with Fouriers law where the heat flux is inversely proportional to material thickness. As the sinter heats its

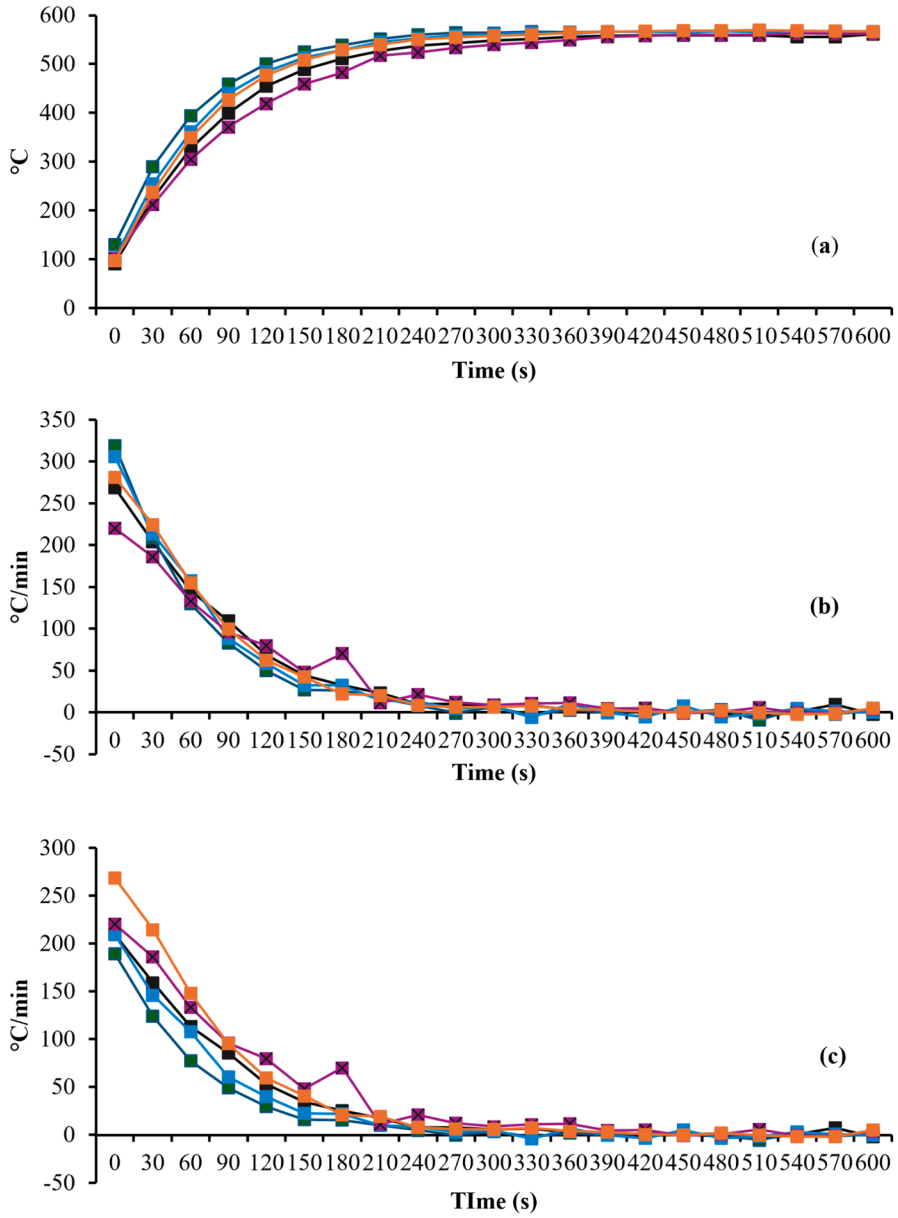

Fig. 6. Steady state furnace set at 600 °C Orange = EC100, Purple = EC75, Blue EC50, Green = EC25, Black = EC0 where a = Temperatures recorded every 30 s b = Temperatures recorded every 30 s c = heating rate adjusted for volume calculated in 30 s intervals.

Table 4
Dimensions of selected sinter samples as measured on Image J where the subscripts a and b refer to panels A and B in Fig. 1.

Sample	$Area_a$ mm^2	$Width_b$ mm	$Volume_a$ mm^3	$Area_b$ mm^2	$Height_a$ mm	$Volume_b$ mm^3
0	665	19	12526	529	22	11409
25	520	21	10876	477	19	8897
50	765	19	14577	654	21	13767
75	543	23	12536	567	18	10034
100	762	26	19673	700	22	15391

composition becomes more similar as the complex phases begin to break down. Average heating rates varied by a maximum of 2 °C/min proving that the only variation in the heating rate of the samples was during the initial stages. In these initial stages, the data showed EC25 being consistently low and EC75 was consistently high. Firstly, due to its balance of FeO to Fe_2O_3 enabling it to maintain high heating rates as the temperature increased; and secondly, because of its high proportion of SFCA which assisted in the conduction of heat between the phases.

Table 5
Results of the emissivity tests where T = Furnace temperature, ϵ = emissivity and the standard deviation °C is given in parentheses.

		Maximum Temperature °C					
T °C	ϵ	EC0	EC25	EC50	EC75	EC100	Average °C
200	0.82	202	200	199	200	204	201 (2.0)
300	0.89	293	301	308	307	296	301(6.7)
400	0.88	406	403	401	399	398	402 (3.1)
500	0.92	492	496	507	505	503	500 (6.3)
600	0.93	601	599	603	599	603	601 (2.0)

3.3. Firebox

The results of the firebox tests are displayed in Fig. 7a-c and show the

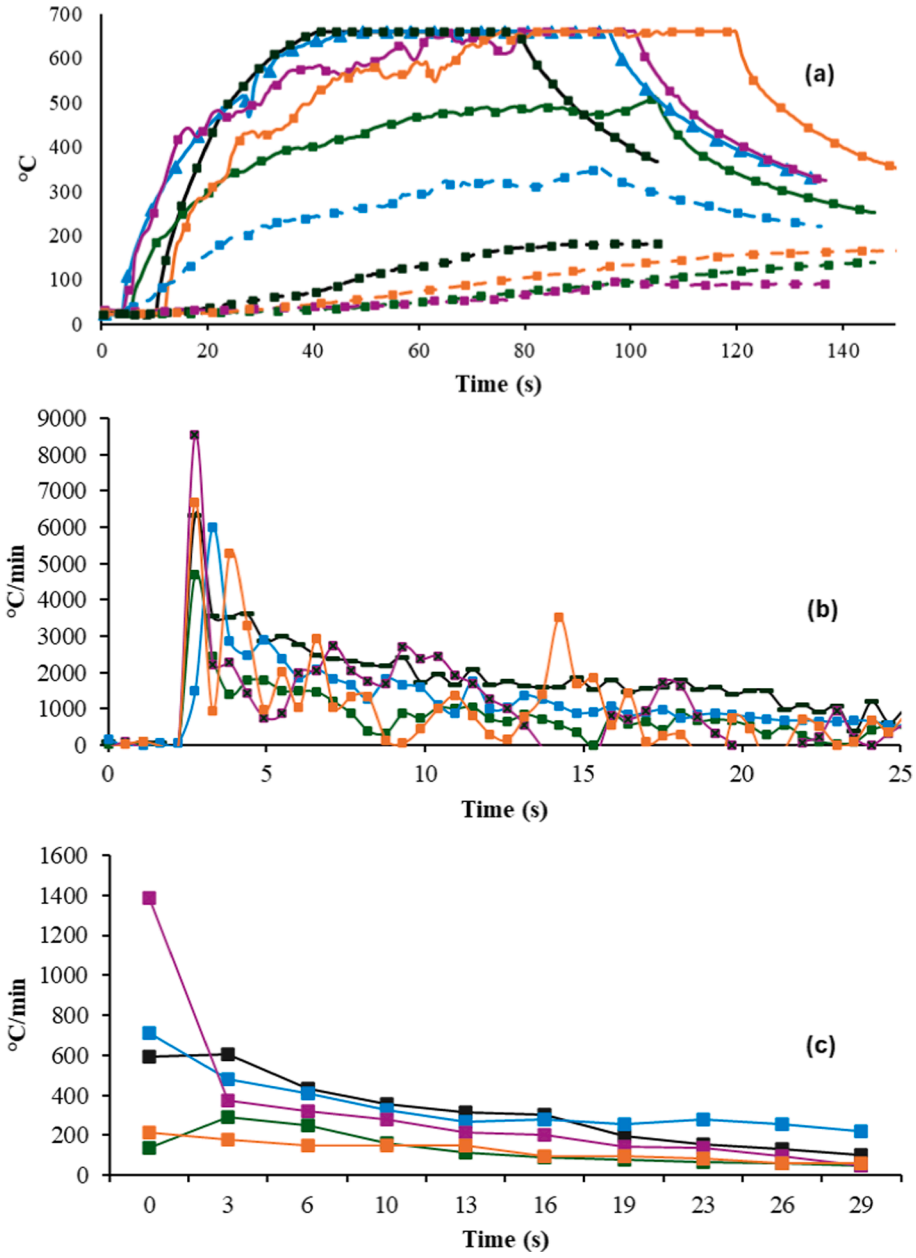

Fig. 7. Firebox tests where Orange = EC100, Purple = EC75, Blue = EC50, Green = EC25, Black = EC0. a= Temperature at the flame contact point (solid) and at point furthest from the flame (dotted) b= heating rate at the flame contact point c= Average heating rate at increasing distance from the flame contact poitn.

temperature, heating rate at the flame contact point and average heating rate vs distance. Heat transfer at the flame contact point was so extreme that the temperature limit of the camera was exceeded, as seen in Fig. 7a. Fig. 7b shows, as expected, very high heating rates within the samples, especially at the flame contact point with instant heating rates in the order of 5000-9000 °C/min. Propane combustion at ca. 2000 °C released large amounts of radiant heat transferred within hot combustion products CO_2 and H_2O. These compounds both rapidly emit large quantities of infrared photons, further enhancing heat transfer from the combustion event to the sinter. However, the average heating rates shown in Fig. 7c were much lower with values of 100-400 °C/min.

Fig. 7b, showed that EC75 had the highest heating rate at the flame contact point at t = 0 followed by EC50 and EC0 mirroring the results of the furnace tests. As time elapsed, the heating rate of EC0 and EC50 remained high while EC75 reduced and EC25 and EC100 remained consistently low. The length of the sinter, measured using ImageJ, was used to calculate how the average heating rate varied with distance from the flame Fig. 7c. The data showed that EC0 and EC50 had the highest heating rates along the whole length of the sample, correlating well with the instant heating rates. Once again, EC25 and EC100 had consistently low heating rates. These results demonstrated the exponential effect that distance had on the heating rate. Furthermore, the oscillating between heating and cooling further into the test reflected the high emissivity of the sinter. Comparing the results from the furnace tests, the EC50 and 75 blends were consistent in their high heating rates along with EC25 and 0 in their low heating rates. Thus validating the effect of oxide distribution on the conductive properties of the sinter.

3.4. Hotplate

The results of the powder hotplate tests in Fig. 8a-b and 9a-b show the average temperature and heating rate across the samples at 400 °C and 550 °C. Firstly, at 100 s with the hotplate set at 400 °C, the average temperature, Fig. 8a, had a range of 329 °C-315 °C (4.5 %). The

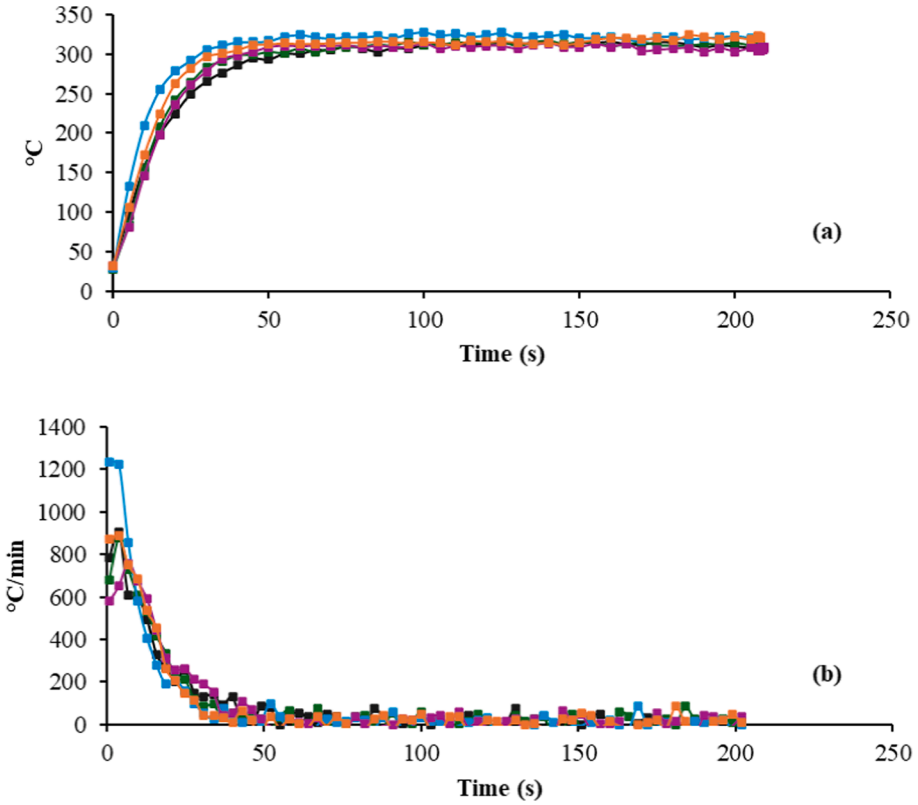

Fig. 8. Samples placed on the hot plate at 400 °C, Orange = EC100, Purple = EC75, Blue = EC50, Green = EC25, Black = EC0 where a = Temperature b = heating rate.

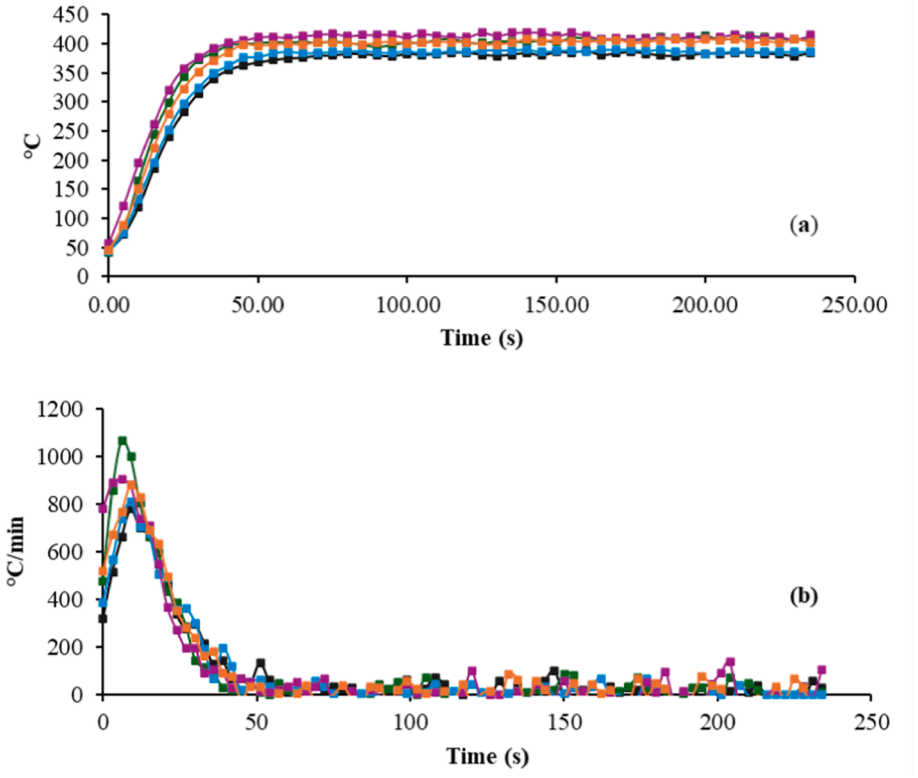

Fig. 9. Samples placed on the hot plate at 550 °C, Orange = EC100, Purple = EC75, Blue = EC50, Green = EC25, Black = EC0 where a = Temperature b = heating rate.

temperature data showed that thermal equilibrium with the hotplate was never achieved because the sinter rapidly radiated energy to the atmosphere. This was observed as pulsing on the thermal image as the sample heated and cooled repeatedly. A similar phenomenon was observed in the firebox tests at thepoints furthest from the flame, backing up the evidence that sinter made with ecoke® has a high emissivity and thermal conductivity. It was clear from the data that EC50 consistently had the highest temperature and EC0 the lowest in opposition to the 550 °C tests where EC75 had the highest temperature. Despite this, the trend for the other samples remained consistent where EC100 reached the second highest temperature followed by EC25 and then EC75.

Analysing the heating rates in Fig. 8b, EC50 had the highest peak heating rate and EC75 the lowest, although this changed as the heating continued. At 20 s, EC50 had dropped to the lowest heating rate and EC100 claimed the top spot, though by 30 s EC75 achieved the highest heating rate. Lastly, by 40 s, the trend had changed again with EC0 having the highest heating rate. These results demonstrate a significant variance, indicating that without the limitations of morphology, the SFCA phases had a good correlation with the heating rate with R scores > 0.8. Further to this, the dense type had an almost perfect R score of $R = 0.99$, at 40 s. The quantity of FeO and total Fe also had a good correlation with maximum R scores of 0.77 and 0.76 at 40 s.

Looking at the 550 °C tests in Fig. 9a, the average temperature of EC75 reached a maximum of 422 °C while EC0 only reached 391 °C. This equates to a difference of 7.9 %, almost double that of the 400 °C tests. At 20 s into heating, the trend was the same with EC75 having the highest temperature followed by EC25, EC100, EC50 and EC0. This trend remained the same throughout the heating. These results show that when the morphology of the samples was the same the variability between the samples increased at higher temperatures. The change in the maximum observed temperature correlates to the variance in emissivity between the samples caused by differing compositions.

Analysing the heating rate showed a slight difference to the 400 °C test where EC25 had the highest peak heating rate, followed by EC75, EC100, EC50 and EC0. Further into the heating, at 20 s, EC75 had a significantly lower heating rate than the other samples with a 72 °C/min gap between it and the next lowest heating rate, whilst the remaining four samples only had 16 °C/min between them. Fig. 9b shows the magnitude of the heating rate decreased rapidly with the peak values having an average of 920 °C/min while after 20 s the average reduced to 515 °C/min. Overall,heating rates had a difference of 24 °C/min (9 %), calculated at 75 s from the start, with EC25 having the highest, followed by EC75, EC100, EC50 and EC0.

3.5. Statistical analysis

To enable a comparison between the samples over the entire heating range their sum was calculated, to correct for any outlying values. A normalization procedure using the same premise as equations (2) and (3), where all the values in a frame are divided by the highest value in that frame, was then applied. The results with and without normalisation were subsequently compared. Both analysis methods showed similar trends therefore, subsequent discussion will refer to both unless stated. The firebox showed a clear downward trend from EC0 to EC100 from 0 to 10 mm from the flame contact point, indicating a reduced conductivity with increasing ecoke® addition. The average heating rates showed the same trend at 10 mm but at 0 mm there was significant variation due to the extreme heating rates involved. The furnace tests at 400 °C had an increasing trend from EC0 to EC75, although EC100 had the lowest value. In the 600 °C experiments there was a downward trend from EC0 but EC75 still had the highest value. Overall, these tests show the variance in thermal properties between sinter samples made with the same ratio of fuel as the two temperatures show different trends apart from EC75. There does not appear to be a significant change in thermal properties from using bio-fuel instead of fossil fuel.

Finally, the results of the hot plate tests showed very little deviation compared to the other experiments. These results indicate that the lump samples had more variance in their heating rates caused by macrostructure at large thermal gradients. However, at low thermal gradients, the changing microstructure was the limiting factor.

4. Conclusion

The experiments in this paper were designed to provide further supporting evidence for the inclusion of bio-fuels in to the energy vector of steelmaking. By analysing the data we have reached the following conclusions.

- The emissivity of iron ore sinter made using ecoke® had a positive correlation with temperature varying between 0.82 and 0.93 from 200 °C-600 °C.
- The average deviation in emissivity between 0–100 % ecoke® was < 2 %
- EC75 had a consistently high heating rate compared to the other samples
- Using XRF and XRD data it was found that FeO, prismatic and the platy SFCA had a quantifiable effect on the heating rate in the furnace and hotplate tests.
- As temperature increased Fe_2O_3 became the main driver of heating rate.
- An increase in thermal gradient increased the affect of morphology on heating rate and reduced the affect microstrucure.

These conclusions validate the use of ecoke® in the sintering process to create a strong and reduceable iron source for the blast furnace capable of efficient energy transfer while offsetting up to 30 % of fuel emissions.

5. AI Writing statement

During the preparation of this work the author(s) used [Grammarly (free version)] in order to [Review spelling and grammar]. After using this tool/service, the author(s) reviewed and edited the content as needed and take(s) full responsibility for the content of the publication.

Funding

We gratefully thank EPSRC and Tata Steel for co-sponsoring an iCASE PhD studentship (Voucher # 20000176) for SR, EPSRC for funding the Sustain Hub (EP/S018107/1) for PJH.

CRediT authorship contribution statement

Sam Reis: Writing – original draft, Visualization, Validation, Methodology, Investigation, Formal analysis, Conceptualization. **Peter J. Holliman:** Writing – review & editing, Validation, Supervision, Project administration, Funding acquisition, Data curation, Conceptualization. **Ciaran Martin:** Writing – review & editing, Supervision, Resources, Project administration.

Declaration of competing interest

The authors declare that they have no known competing financial interests or personal relationships that could have appeared to influence the work reported in this paper.

Data availability

Select images are available in the electronic supplementary information, further Videos and images from the thermal camera are available on request from the corresponding author.

Appendix A. Supplementary data

Supplementary data to this article can be found online at https://doi.org/10.1016/j.fuel.2024.133172.

References

[1] Swalec C, Grigsby-Schulte A. Pedal to the metal: It's time to shift steel decarbonization into high gear. Tech rep, Global Energy Monitor 2023:lants2. https://globalenergymonitor.org/wp-content/uploads/2023/07/GEMSteelP.

[2] Lungen HB, Schmole P. Comparison of blast furnace operation modes in the world. Steel Res Int 2020;91(11):2000182. https://doi.org/10.1002/srin.202000182.

[3] Liu W, Zuo H, Wang J, Xue Q, Ren B, Yang F. The production and application of hydrogen in steel industry. Int J Hydrogen Energy 2021;46(17):10548–69. https://doi.org/10.1016/j.ijhydene.2020.12.123.

[4] W. of Science, Citation report (2024).

[5] Jha G, Soren S. Study on applicability of biomass in iron ore sintering process. Renew Sustain Energy Rev 2017;80:399–407. https://doi.org/10.1016/j.rser.2017.05.246.

[6] Liu Y, Yang J, Wang J, Cheng Z, Wang Q. Energy and exergy analysis for waste heat cascade utilization in sinter cooling bed. Energy 2014;67:370–80. https://doi.org/10.1016/j.energy.2013.11.086.

[7] Zhang H, Dong L, Li H-Q, Chen B, Tang Q, Fujita T. Investigation of the residual heat recovery and carbon emission mitigation potential in a chinese steelmaking plant: A hybrid material/energy flow analysis case study. Sustainable Energy Technol Assess 2013;2:67–80. https://doi.org/10.1016/j.seta.2013.03.003.

[8] Ammar Y, Joyce S, Norman R, Wang Y, Roskilly AP. Low grade thermal energy sources and uses from the process industry in the uk. Appl Energy 2012;89(1):3–20. https://doi.org/10.1016/j.apenergy.2011.06.003.

[9] Zhang X, Chen Z, Zhang J, Ding P, Zhou J. Simulation and optimization of waste heat recovery in sinter cooling process. Appl Therm Eng 2013;54:7–15. https://doi.org/10.1016/j.applthermaleng.2013.01.017.

[10] Loo CE, Matthews LT, O'Dea DP. Lump ore and sinter behaviour during softening and melting. ISIJ Int 2011:930–8. https://doi.org/10.2355/isijinternational.51.930.

[11] Hesih L, Whiteman J. Sintering conditions for simulating the formation of mineral phases industrial iron ore sinter. ISIJ Int 1989;29(1):24–32. https://doi.org/10.2355/isijinternational.29.24.

[12] R. R. Lovel, K. R. Vining, M. Dell 'amico, The infuence of fuel reactivity on iron ore sintering, ISIJ International 49 (2) (2009) 195–202. doi:10.2355/isijinternational.49.195.

[13] Fan X-H, Zhiyun J, Min G, Chen X-L, Qiang L, Jiang T. Influence of preformation process on combustibility of biochar and its application in iron ore sintering. ISIJ Int 2015;55:2342–9. https://doi.org/10.2355/isijinternational.ISIJINT-2015-332.

[14] Zhao J, Loo C, Yuan J, Wang F, Wang J, Zhang H. A fundamental study of the cocombustion of coke and charcoal during iron ore sintering. Energy Fuel 2018;32:8743–59. https://doi.org/10.1021/acs.energyfuels.8b00939.

[15] Pimenta HP, Seshadri V. Characterisation of structure of iron ore sinter and its behaviour during reduction at low temperatures. Ironmak Steelmak 2002;29(3):169–74. https://doi.org/10.1179/030192302225002009.

[16] Hida Y, Okazaki J, Itoh K, Sasaki M. Formation mechanism of acicular calcium ferrite of iron ore sinter. Tetsu-to-Hagaṅe 1987;73(15):1893–900. https://doi.org/10.2355/tetsutohagane1955.73.15_1893.

[17] Umadevi T, Karthik P, Mahapatra PC, Prabhu M, Ranjan M. Optimisation of feo in iron ore sinter at jsw steel limited. Ironmak Steelmak 2012;39(3):180–9. https://doi.org/10.1179/1743281211Y.0000000080.

[18] Al-Haji T. Developments in iron ore sintering using a laboratory scaled development platform, thesis. Science and Engineering 2023. https://doi.org/10.23889/SUthesis.62668.oa. https://cronfa.swan.ac.uk/Record/cronfa62668.

[19] Li Y, Zeng J, Zhang N, Xue Y, Hou Y, Lv X. Preparation, Structure, and Characterization of SFCA-I. Cham: Springer Nature Switzerland; 2024.

[20] K. Zoll, A. Benisek, E. Dachs, V. Kahlenberg, A. Saxer, P. Tropper, J. de Villiers, Stability and calorimetric studies of silico-ferrites of calcium aluminum and magnesium, Journal of the American Ceramic Society 101 (9) (2018) 4193–4202. https://doi.org/10.1111/jace.15567. URL https://ceramics.onlinelibrary.wiley.com/doi/abs/10.1111/jace.15567.

[21] Donskov E, Lyalyuk V, Donskov A. The energy efficiency of blast furnaces. Steel in Translation 2015;45:130–2. https://doi.org/10.3103/S0967091215020047.

[22] Reis S, Holliman PJ, Martin C, Jones E. Biomass-coal hybrid fuel: A route to net-zero iron ore sintering. Sustainability 2023;15(6):54–95. https://doi.org/10.3390/su15065495.

[23] C. Barrat, A. Audouin, G. Auvray, Influence of ambient temperature on the radiation of ir reference sources: effect on the calibration of ir sensors and method of compensation, in: Electro-Optical and Infrared Systems: Technology and Applications XV, Vol. 10795, SPIE, 2018, pp. 186–194. https://doi.org/10.1117/12.2325369.

[24] Avdelidis NP, Moropoulou A. Emissivity considerations in building thermography. Energ Buildings 2003;35(7):663–7. https://doi.org/10.1016/S0378-7788(02)00210-4.

[25] Usamentiaga R, Molleda J, Garcia D, Bulnes F. Monitoring sintering burn-through point using infrared thermography. Sensors 2013;13:10287–305. https://doi.org/10.3390/s130810287.

[26] De Castro JA, Sazaki Y, Yagi J-I. Three dimensional mathematical model of the iron ore sintering process based on multiphase theory. Mater Res 2012;15:1045–53. https://doi.org/10.1590/S1516-14392012005000107.

[27] Zhang J, Bai H, Wei W, Ding Y, Zhang X, Yuan H, et al. The effect of microstructure on the middle and short waveband emissivity of cuo-doped cuxco1-xfe2o4 spinel. J Alloy Compd 2019;787:638–48. https://doi.org/10.1016/j.jallcom.2019.02.119. https://www.sciencedirect.com/science/article/pii/S0925838819305596.

[28] Huang H, Yang Y, Zhu Y. Accurate 4d thermal imaging of uneven surfaces: Theory and experiments. Int J Heat Mass Transf 2023;216:124580. https://doi.org/10.1016/j.ijheatmasstransfer.2023.124580. https://www.sciencedirect.com/science/article/pii/S0017931023007251.

[29] Bassi PS, Gurudayal LH, Wong J. Barber, Iron based photoanodes for solar fuel production. Phys Chem Chem Phys 2014;16:11834–42. https://doi.org/10.1039/C3CP55174A.

[30] Pham HL, Nguyen VD, Nguyen VK, Le THP, Ta NB, Pham DC, et al. Rational design of magnetically separable core/shell fe3o4/zno heterostructures for enhanced visiblelight photodegradation performance. RSC Adv 2021;11:22317–26. https://doi.org/10.1039/D1RA03468E.

[31] Zhang S, Li K, Ma Y, Guo F, Jiang C, Liang Z, et al. Density functional studies on the atomistic structure and properties of iron oxides: A parametric study. Materials 2022;15(23). https://doi.org/10.3390/ma15238316.